Aalborg Universitet

AALBORG UNIVERSITY

DENMARK

Neural network-aided 4-DF global efficiency optimal control for the DAB converter based on the comprehensive loss model

Zhang, Hao; Tong, Xiangqian; Yin, Jun; Blaabjerg, Frede

Neural network-aided 4-DF global efficiency optimal control for the DAB converter based on the comprehensive loss model

Hao Zhang [a], Xiangqian Tong [a,**], Jun Yin [a], Frede Blaabjerg [b,*]

[a] School of Electrical Engineering, Xi'an University of Technology, Xi'an, China
[b] Department of Energy Technology, Aalborg University, Aalborg, Denmark

A R T I C L E   I N F O

A B S T R A C T

—Intending to enhance the efficiency of dual-active-bridge (DAB) converters, this paper presents a four degree-of-freedom (DF) efficiency optimization method based on the comprehensive loss model. Besides the traditional triple-phase-shift modulation, the switching frequency is added as another control DF to minimize the core loss of the high-frequency transformer (HFT). Considering the nonlinear characteristics of the switching devices and the HFT, the comprehensive loss model is established first to reflect the converter's overall loss directly. Then the algorithm-based efficiency optimization solution is proposed to investigate the 4-DF modulation variables, which are subject to the minimal overall loss of the DAB converter in a given operating condition. A neural network (NN) is then adopted to model the mapping relationship between the ideal 4-DF variables and the working conditions. On this basis, a closed-loop controller that combines the traditional PI regulator and the NN module is suggested to realize both the output target control and the efficiency optimization. Finally, the performance of the proposed control strategy is fully verified through a 1.2 kW experimental prototype. The experimental results show that the converter's efficiency is significantly improved with the NN-aided 4-DF control strategy.

1. Introduction

As the framework and technical basis in the energy internet industry, the intelligent microgrid provides a promising solution for distributed energy resources access and optimal energy allocation in renewable-based power systems [1]. Fig. 1 shows a typical AC/DC hybrid microgrid scenario, in which the isolated bidirectional DC-DC converter plays a significant role in power flowing and DC voltage control, where the converter's efficiency is always an essential concern [2,3]. Due to the concise structure and zero-voltage switching (ZVS) characteristics, the dual active bridge (DAB) converter has become a highly attractive topology for the isolated bidirectional DC-DC converter [4].

DAB converter can operate under several modulation strategies with different degree-of-freedom (DF). The single-phase-shift modulation method with 1 DF is the simplest [5], but the ZVS may be lost under light-load conditions. Moreover, when the converter operates in a wide input/output voltage range, the current stress will increase, leading to a remarkably low efficiency [6]. To enhance the efficiency and performance of DAB, the more complex and also the most representative strategy, the triple-phase-shift (TPS) modulation with 3 DF, has been

studied [7–9]. Different combinations of the three phase-shift ratios are selected in TPS modulation to shape the inductor current of the high-frequency AC link, typically aiming to optimize a loss-related objective function. Most existing studies have adopted one or more indirect optimization objects, such as ZVS [6,7], current stress [8–10], reactive power [11,12], etc.

The implementation of ZVS can significantly reduce the converter's switching loss. A current-based ZVS analysis method, which judges the ZVS realization according to the current direction at the switching time, was used in most studies due to simplicity. However, current-based ZVS has a low accuracy. As an improvement, an energy-based ZVS analysis method was proposed in Ref. [6], which considers the optimal charging amount of power devices' parasitic capacitance in the switching process. In Ref. [7], a switchable-series-inductor structure is used to replace the traditional single inductor, which improves the efficiency of the converter under light-load conditions, but the circuit structure is more complex.

Minimizing the current stress can reduce the converter's conduction loss. In Ref. [8], ant colony optimization (ACO) is used to optimize the peak inductor current. Compared with the peak value, the root-mean-square (RMS) inductor current value can reflect the

Nomenclature

Abbreviations

DF	Degree-of-freedom
HFT	High-frequency transformer
TPS	Triple-phase-shift
ZVS	Zero-voltage switching
NN	Neural network
TS	Traversal search
CS	Cuckoo search
CV	Constant-voltage
CP	Constant-power
VAPL	Variable-amplitude power limiter

Indices

n	Subscript, index of the normalized values
g	Subscript, index of the given values
x	Subscript, index of the sequence number
S_x	Index of the xth semiconductor switch, $x \in [1,8]$

Variables

t_x	The xth time node in a half switching period, $x \in [0, 4]$
V_1, V_2	The input and output DC voltage, respectively
V_H	Output voltage of the front-end H-bridge
V_P	Voltage at the primary side of HFT
V_S	Voltage at the secondary side of HFT
v_L	Voltage across the inductor L.
v_{Px}, v_{Lx}	Values of v_P and v_L from t_{x-1} to t_x, respectively
v_{DSx}	The drain-source voltage value of S_x
i_L	Current through the inductor L.
$i_L(t_x)$	The instantaneous inductor current value at t_x
I_{Lrms}	The root-mean-square value of the current i_L.
C_{px}	Junction capacitance of the switch S_x. The value of C_{px} varies with the voltage v_{DSx}
T_s	The switching period
D_1	Inner phase-shift ratio of HB_1, $D_1 \in [0, 1]$
D_2	Inner phase-shift ratio of HB_2, $D_2 \in [0, 1]$
D_3	Outer phase-shift ratio, $D_3 \in [-1, 1]$
M	DC voltage gain
M_g	DC voltage gain at a given operating point
P_{max}	The maximum power transmission value
P_n	Normalized power value by the rated power
P_g	Power transmission at a given operating point
P_{LossO}	Conduction loss of the switches
P_{LossW}	Winding loss of the transformer
P_{LossA}	Total switching loss of all switches
P_{LossB}	Magnetic hysteresis loss of the transformer
P_{LossC}	Total conduction loss, which is a sum of P_{LossO} and P_{LossW}
P_{Loss}	The comprehensive loss, which is a sum of P_{LossA}, P_{LossB}, and P_{LossC}

conduction loss more accurately. Ref. [9] proposes a modulation strategy to minimize the RMS current through partial derivatives. In Ref. [10], a deep-reinforcement-learning-based strategy is proposed to minimize the RMS current and also realize the ZVS, but the parasitic capacitance of the switching devices is not considered. In addition, Refs. [13,14] adopt a 5-DF modulation strategy (TPS plus two duty cycles of the H-bridges) to broaden the ZVS range and minimize the current stress. Compared with the TPS modulation, the converter's operating mode is more generalized, but the converter's efficiency under heavy-load conditions is not improved.

Minimizing the reactive power in the high-frequency AC link is another way to improve the converter's efficiency. Aiming at reducing the reactive power of DAB under TPS modulation, Refs. [11,12] respectively provide a particle swarm optimization (PSO) method and a deep reinforcement learning method to investigate the optimal TPS modulation parameters. However, some reactive power is necessary to achieve full ZVS, so minimizing the reactive power may cause an increase in the switching loss.

Besides the switching loss and conduction loss, core loss of the high-frequency transformer (HFT) is another significant component of the converter's comprehensive loss. However, in the indirect loss-related methods mentioned above, the loss of the HFT is often neglected, which is unfavorable for improving the overall efficiency of DAB.

Consequently, it is necessary to improve the overall efficiency by directly optimizing the comprehensive loss for the DAB converter. A hybrid modulation strategy combining dual-phase-shift and frequency-adjustment is proposed to minimize the total loss of DAB in Ref. [15]. Nevertheless, the dual-phase-shift modulation rather than TPS modulation is adopted, and the parasitic capacitance of the switching devices is not considered in the switching loss model, leading to limited
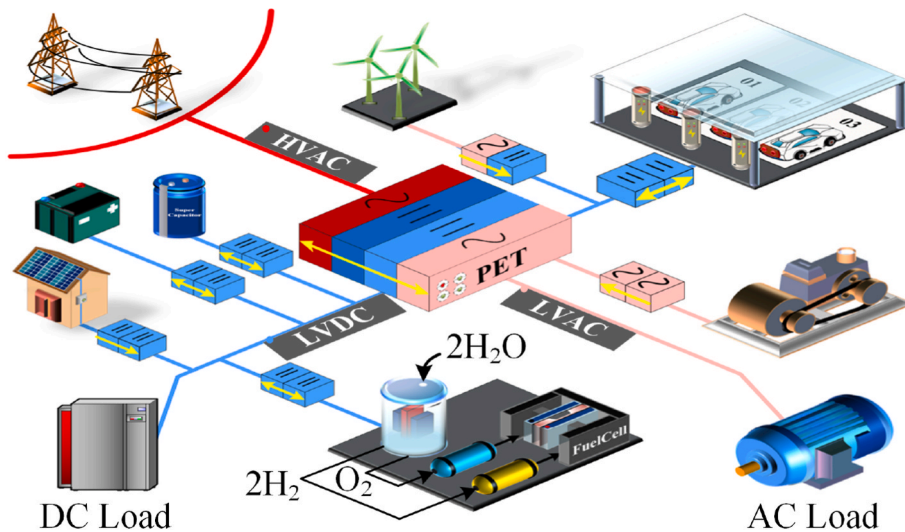

Fig. 1. Typical AC/DC hybrid microgrid application scenarios with isolated bidirectional DC-DC converters.

efficiency. In fact, the minimization of the comprehensive loss is more complex with the increase of DF.

To further improve the overall efficiency of the converter in a wide operating range, this paper proposes a direct optimization method based on the comprehensive-loss function and 4-DF modulation strategy combining TPS and frequency adjustment. The comprehensive loss model has considered the nonlinear characteristics of the switch parasitic capacitance and the HFT excitation inductance. An integrated solving framework that combines optimization algorithm and NN fitting is introduced to attain the optimal operating data, model the nonlinear relationship between the ideal 4-DF parameters and the working condition variables, and then provide 4-DF schemes with the best efficiency for the DAB converter in a continuous operating range.

In addition, to ensure the robust and economical operation of the microgrid, the energy-management controller will make necessary adjustments to the DC bus voltage or power flow [16,17]. Hence, the DAB converter must be closed-loop controlled. Based on the proposed 4-DF modulation, an NN-aided closed-loop controller is proposed to track the voltage/power commands and improve the converter's efficiency synchronously. The test results of the experimental prototype show that the NN-aided 4-DF global efficiency optimal control strategy is effective and feasible.

2. Operating mechanism and the efficiency optimization problem of the DAB converter

Fig. 2 shows the power circuit diagram of the DAB converter and its operating waveforms under TPS modulation, where L is the auxiliary inductor, and HB_1 and HB_2 are the H-bridges on the input and output sides, respectively. S_x denotes the semiconductor switch that consists of active switch T_x, the body diode D_{px}, and the junction capacitance C_{px}. V_1 and V_2 are the DC voltages at the input and output sides, respectively. V_H is the output voltage of HB_1, and V_P and V_S are the voltages on the primary and secondary sides of the HFT, respectively. N_T is the voltage transmission ratio of the HFT.
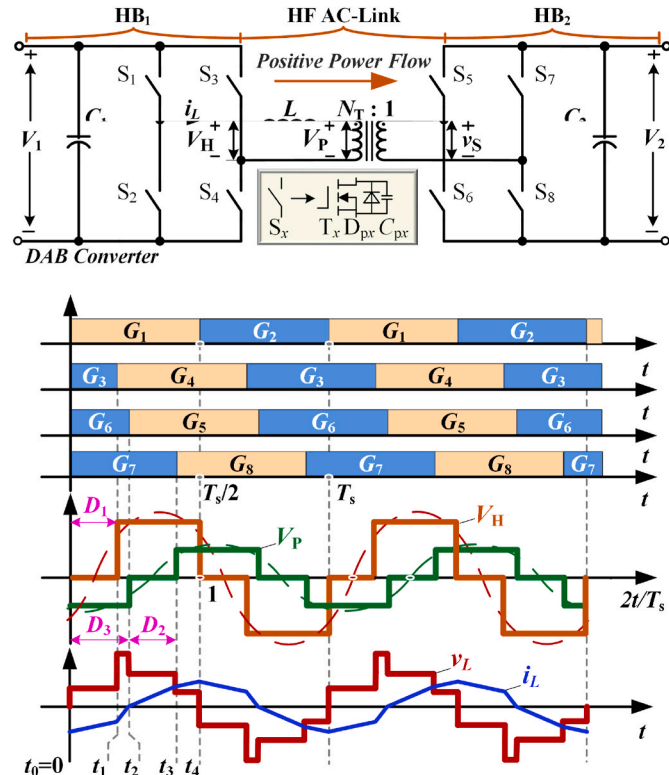

Fig. 2. DAB converter and its waveforms under TPS modulation.

Under TPS modulation, the switch S_x is driven by the square-wave signal G_x with a period of T_s. $D_1 \in [0, 1]$ (corresponding to a phase angle varying from 0 to π), $D_2 \in [0, 1]$, and $D_3 \in [-1, 1]$ are the inner phase-shift ratio of HB_1, HB_2, and the outer phase-shift ratio between the two HBs, respectively. Specifically, the phase-shift time between S_1 and S_4, S_5 and S_8, S_1 and S_5 is $D_1T_s/2$, $D_2T_s/2$, and $D_3T_s/2$, respectively. The indices from t_0 to t_4 are the jumping time nodes of the inductor voltage v_L. Different values of D_1, D_2, and D_3 classify the state of the converter into 12 operating modes, of which the six modes of $D_3 \in [0,1]$ are described in detail in Fig. 3 and Table 1.

In Table 1, $M = N_T V_2/V_1$ is the equivalent DC voltage gain, and the subscript n is the symbol for normalized values. The variables from t_{1n} to t_{3n} are the time-node values normalized by $T_s/2$ ($t_{0n} = 0$ and $t_{4n} = 1$ are omitted). To evaluate the switching loss, it's necessary to calculate the inductor current at each time node:

$$\begin{cases} i_L(t_0) = -i_L(t_4) \\ i_L(t_x) = i_L(t_{x-1}) + (t_x - t_{x-1})v_{Lx}/L, x \in \{1, 2, 3, 4\} \end{cases} \quad (1)$$

where v_{Lx} denotes the constant inductor voltage from t_{x-1} to t_x. The values of v_{Lx} normalized by V_1 are listed in Table 1. In addition, the RMS value of i_L is also deduced as

$$I_{Lrms} = \sqrt{\frac{2L}{3T_s} \sum_{x=1}^{4} \frac{\left[i_L(t_{x-1}) + \frac{v_{Lx}t_x}{L}\right]^3 - \left[i_L(t_{x-1}) + \frac{v_{Lx}t_{x-1}}{L}\right]^3}{v_{Lx}}} \quad (2)$$

which is used to calculate the conduction loss of the switches and the copper loss of the HFT. Besides, the uniform expression of the system power transmission is derived as

$$P_S = \frac{1}{T_s} \sum_{x=1}^{4} \left\{ v_{Px}(t_x - t_{x-1}) \left[2i_L(t_{x-1}) + v_{Lx}\frac{t_x - t_{x-1}}{L} \right] \right\} \quad (3)$$

The maximum forward power transmission occurs when (D_1, D_2, D_3) = (0, 0, 0.5), and the maximum value of P_S is

$$P_{max} = \frac{MV_1^2 T_s}{8L} \quad (4)$$

The global power distribution diagram of DAB with TPS modulation is shown in the left inset of Fig. 4, where the values of P_{Sn} (P_S normalized by P_{max}) are distinguished by color. Several groups of equal-power points are extracted from the left inset and form the isosurfaces in the right inset of Fig. 4 ($P_{Sn} = -0.2$ in black, $P_{Sn} = 0.3$ in blue, $P_{Sn} = 0.7$ in red, and $P_{Sn} = 0$ in four translucent planes).

It can be seen that on each power isosurface, there are massive combinations of the phase-shift modulation variables, of which an optimal scheme with the minimum overall loss needs to be explored. Considering the frequency modulation, the efficiency optimization problem of DAB is expressed as follows:

$$\min P_{Loss}(f, D_1, D_2, D_3) \quad (5)$$

$$\text{s.t. } P_S(f, D_1, D_2, D_3)|_{M=M_g} = P_g \quad (6)$$

where P_{Loss} is the comprehensive loss of the DAB converter, f is the switching frequency, and M_g and P_g are the certain values of the DC voltage gain and power transmission at a given operating point, respectively. Detailed analysis and calculation method of P_{Loss} is introduced in Section 3.

3. Comprehensive loss model of DAB

The comprehensive loss mainly includes the loss of the switching devices and the HFT.
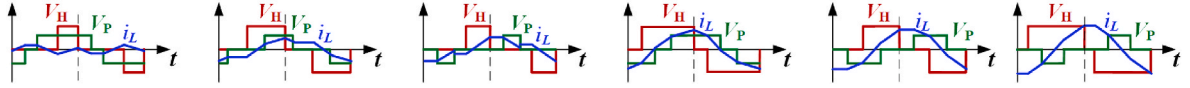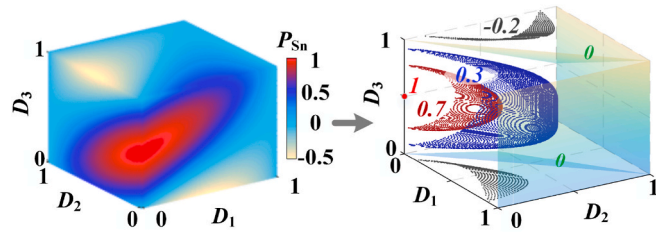
Fig. 3. General working waveforms of each operating mode of the DAB converter.

Table 1
Pivotal information of the operating modes.

Mode	t_{1n}	t_{2n}	t_{3n}	v_{L1n}	v_{L2n}	v_{L3n}	v_{L4n}	v_{H1n}	v_{H2n}	v_{H3n}	v_{H4n}
1	D_3	$D_2 + D_3$	D_1	M	0	$-M$	$1-M$	0	0	0	1
2	D_3	D_1	$D_2 + D_3$	M	0	1	$1-M$	0	0	1	1
3	$D_2 + D_3$-1	D_3	D_1	0	M	0	1	0	0	0	1
4	D_1	D_3	$D_2 + D_3$	M	$1 + M$	1	$1-M$	0	1	1	1
5	$D_2 + D_3$-1	D_1	D_3	0	M	$1 + M$	1	0	0	1	1
6	D_1	$D_2 + D_3$-1	D_3	0	1	$1 + M$	1	0	1	1	1

Fig. 4. Normalized power (P_{sn}) distribution under TPS modulation.

3.1. Loss of the switches

Take the calculation of switching loss of power devices at t_1 in Fig. 2 as an example. Fig. 5 (a) shows the equivalent circuit diagram of HB_1 from t_1 to t_d, where $[t_1, t_d]$ is the dead-time between the driving signals G_3 and G_4. S_3 turns off at t_1, where the energy exchange between capacitors C_{p3} and C_{p4} starts. The voltage v_{DS4} drops to a lower value (ideally 0) at t_d. Considering the nonlinear relationships between the junction capacitance and the drain-source voltages shown in Fig. 5 (b), the values of v_{DS3} and i_L during the dead time $[t_1, t_1+t_d]$ can be calculated by the following iterative expressions:

$$\begin{cases} v_{DS3}(t + \Delta t) = v_{DS3}(t) + \left(A_f \omega_f e^{\omega_f \Delta t} - B_f \omega_f e^{-\omega_f \Delta t} \right) \Delta t \\ \omega_f = 1 / \sqrt{2LC_{p3}} \\ A_f = \left[-i_L(t_1) \sqrt{0.5L/C_{p3}} - v_P(t) \right] / 2 \\ B_f = -v_P(t) - A_f \end{cases} \tag{7}$$

$$i_L(t + \Delta t) = i_L(t) + [v_{DS3}(t) - v_P(t)] \Delta t / L \tag{8}$$

where Δt is the calculation step size, which should be far less than the resonant period $2\pi/\omega_f$. In this illustrated case, a negative value of $i_L(t_1)$ is necessary to realize the ZVS of S_4. After iterative calculation, the switching-off current of S_3, namely $i_L(t_1)$, the switching-on voltage of S_4,
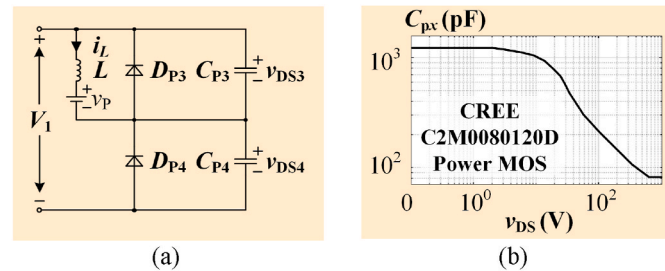
namely $v_{DS4}(t_d)$, and the switching-on current of S_4, namely $i_L(t_d)$ can be obtained. Consequently, the switching loss of S_3 and S_4 can be calculated by the following formula (9).

$$P_{Loss\,(3,4)} = f \cdot \left[V_1 |i_L(t_1)| t_f + v_{DS4}(t_d) |i_L(t_d)| t_r \right] / 3 \tag{9}$$

where $P_{Loss\,(3,4)}$ denotes the switching loss produced by S_3 and S_4, t_r represents the rise time of the switching-on current of S_4, and t_f represents the fall time of the switching-off current of S_3. The values of t_r and t_f can be approximated by looking in the devices' datasheet. Since the turn-off time of S_3 always equals to $D_1 T_s/2$ among all operating modes, the value of $i_L(t_1)$ can be easily obtained by (1), and formula (9) can be applied to all operational modes. The calculation methods of the switching loss produced by other switches, namely $P_{Loss\,(1,2)}$, $P_{Loss\,(5,6)}$, and $P_{Loss\,(7,\,8)}$, are similar and will not repeat here. The total switching loss can be expressed as

$$P_{LossA} = \sum P_{Loss(x,x+1)} \big|_{x=1,3,5,7} \tag{10}$$

Regardless of the dead-time, there are always four switches in conducting state. Therefore, the conduction loss of the switching devices is expressed as:

$$P_{LossO} = 4 I_{Lrms}^2 R_{on} \tag{11}$$

where R_{on} is the on-state resistance of each switch. Finally, the loss of the switches is a sum of P_{LossA} and P_{LossO}.

3.2. Loss of the HFT

The loss of HFT is mainly composed of core loss and copper loss. The simplified circuit scheme of the HFT is shown in Fig. 6 (a), where L_s is the leakage inductance, L_m is the excitation inductance, and R_{w1} and R_{w2} are the equivalent resistance of the windings.

Ref. [18] provides an improved method for the core loss calculation of HFT excited by square voltages, which is expressed as

$$P_{LossB} = \frac{2^{\alpha+\beta}(1-D_2)^{1-\alpha} K V_c \rho_s f^\alpha B_m^\beta}{(2\pi)^{\alpha-1} \int_0^{2\pi} |\cos \theta|^\alpha 2^{\beta-\alpha} d\theta} \tag{12}$$

where K, α, and β are the Steinmetz coefficients, which can be established from the core datasheet, B_m is the peak-magnetic-induction, V_c is the magnetic core volume, and ρ_c is the core density. The peak-magnetic-induction is directly related to the peak-excitation-current, which is derived as

$$i_{emax} = \int_{D_3 T_s/2}^{(D_3+1)T_s/2} \frac{[v_P(t) + L_s d i_L(t)/dt]}{2L_M} dt \tag{13}$$

After substituting v_P to formula (13), the peak-excitation-current can

Fig. 5. (a) Equivalent circuit diagram of HB_1 during the energy exchanging process between S_3 and S_4. (b) Nonlinear parasitic output capacitance C_P (v_{DS}) of the using MOSFETS.
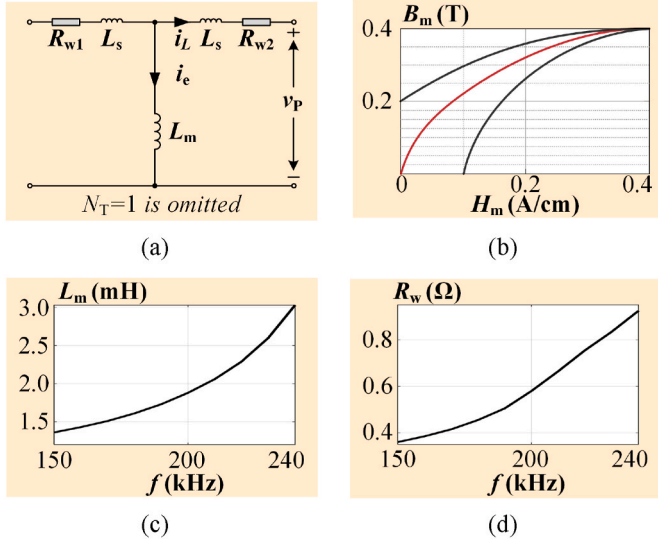
(a)

(b)

(c)

(d)

Fig. 6. Circuit diagram and features of the HFT. (a) Simplified circuit diagram. (b) *B–H* curve. (c) Variation curve of the excitation inductance with frequency. (d) Variation curve of the winding resistance with frequency.

(a)

(b)

(c)

(d)

Fig. 7. Distribution diagrams of (a) P_{LossA}, (b) P_{LossB} and (c) P_{LossC} on power isosurface $P_{Sn} = 0.48$ in the TPS space. (d) Variation curves of the minimum values of different losses with the switching frequency.

be simplified as (14):

$$i_{emax} = \frac{MV_1(1 - D_2)}{4fL_m} + \frac{L_s}{L_m}i_L(D_3T_s / 2) \qquad (14)$$

by which the magnetic field strength H_m can be obtained:

$$H_m = Ni_{emax}/l_e \qquad (15)$$

where N is the secondary winding turns, and l_e is the length of the magnetic path. Then the value of B_m can be determined by the hysteresis loop curve shown in Fig. 6 (b). Fig. 6 (c) shows that the value of L_m increases when the frequency rises, which may lead to decreases of i_{emax} and B_m according to (14), (15), and Fig. 6 (b). Therefore, the core losses may reduce when f increases within moderate limits [15].

The copper loss of the transformer can be expressed as

$$P_{LossW} = I_{Lrms}^2 R_w \qquad (16)$$

where R_w is the total winding resistance. Due to the skin effect and proximity effect, the equivalent winding resistance increases with the frequency increase. This paper uses a frequency-impedance tester to directly measure the variation of R_w with f, as shown in Fig. 6 (d). Finally, the loss of the HFT is a sum of P_{LossB} and P_{LossW}.

3.3. Comprehensive loss model of DAB

Consequently, the comprehensive loss of the DAB converter is expressed as

$$\begin{cases} P_{LossC} = P_{LossO} + P_{LossW} = I_{Lrms}^2(4R_{on} + R_w) \\ P_{Loss} = P_{LossA} + P_{LossB} + P_{LossC} \end{cases} \qquad (17)$$

where P_{LossC} is defined as the total conduction loss of the converter. The comprehensive loss P_{Loss} is a sum of the switching loss, the core loss and the total conduction loss. Formula (2) and Table 1 suggest that the value of I_{Lrms} is determined by the modulation parameters f, D_1, D_2, and D_3. Therefore, the total conduction loss P_{LossC} is a function of (f, D_1, D_2, D_3). Similarly, P_{LossA} and P_{LossB} are also related to the 4-DF parameters. Hence, the comprehensive loss P_{Loss} is a function of (f, D_1, D_2, D_3), which is consistent with the expression in (5).

Fig. 7 (a) to (c) show the distributions of different losses under the condition of $V_1 = 200$ V, $M = 1.5$, $P_s = 600$ W with $f = 150$ kHz. Fig. 7 (b)
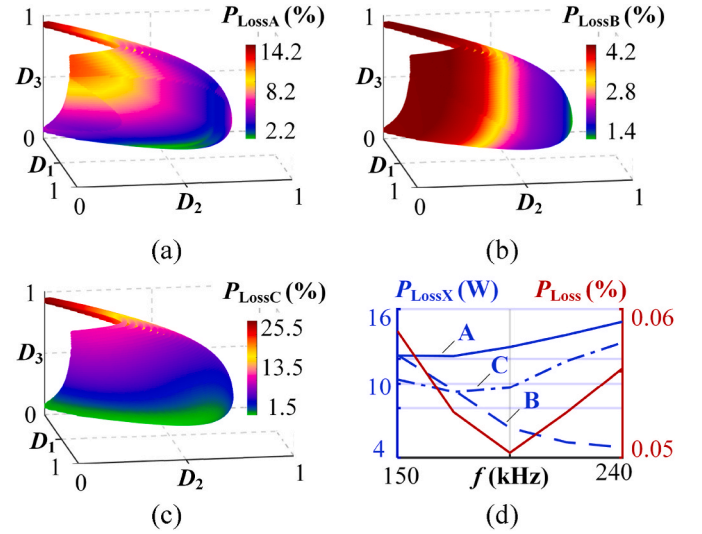
shows that P_{LossB} is inversely proportional to D_2, which is consistent with formulas (13) and (14). Obvious contrasts of peak-valley values of the losses indicate the necessity of optimizing the TPS ratios.

Fig. 7 (d) is obtained by the traversal search (TS) method, where the variation curves of the lowest total loss and its components with the switching frequency are described. Specifically, the variation curves of P_{LossA}, P_{LossB}, P_{LossC}, and the total loss percentage are described by the blue line, the blue dotted line, the blue chain line, and the red line, respectively. With the frequency rise, P_{LossA} and P_{LossC} increase slowly while the core loss P_{LossB} decreases, leading to the overall loss changes first declining and then an upward trend, where the peak-valley value of P_{Loss} is almost one percent, which shows the necessity of frequency modulation.

Nevertheless, the traversal search is very time-consuming. Thus, this paper utilizes advanced optimization algorithms to investigate the optimal 4-DF parameters in the whole working range of DAB, which is introduced in Section 4.

4. Proposed NN-aided 4-DF control strategy

This section introduces the 4-DF global efficiency optimal control scheme for DAB. Firstly, the efficiency optimization problem shown in (5) and (6) is solved by traversal search and four different algorithms among 4000 steady-state points (40% of the total required number) of DAB. Then, the Cuckoo search with the best performance attains the best 4-DF parameters in the whole operating range, which provides the database for the training and fitting of the NN-aided 4-DF modulation module. Finally, an NN-based closed-loop controller is proposed, which realizes the decoupling between the closed-loop control and the efficiency optimization of the DAB converter.

4.1. Solving method of the efficiency optimization problem

The DC voltage gain M and the power transmission P_S can describe the converter's operating condition. In general, the whole operating range of DAB is set as $M \in [0.5, 2]$ and $P_n \in [0, 1]$, where the upper limit 1 of P_n corresponds to the converter's rated power. Taking a step size of 1% of both M and P_n to describe the whole operating space of DAB discretely, then there is a total of 10000 operating conditions. The frequency range of the employing HFT is [150, 240] kHz, and the search accuracy of the switching frequency is 500 Hz. The search accuracy of the TPS ratios is 0.002, corresponding to a time step of 6.6 ns (half of the

using MOSFET's switching time) under 150 kHz. Multi-variable, high precision brings an enormous solution space. For example, there are more than 30 million possible solutions under each frequency at the operating point $(M, P_n) = (1, 0.4)$, which poses a tremendous challenge in exploring the global optimal solution.

Fig. 8 shows the proposed solving framework for the efficiency optimization problem, of which Step 1 introduces the feasible region constructions of the modulation parameters. The voltage gain M and normalized power P_n change by 1%, respectively, continuously producing different working points. At each given point (M_g, P_g), the frequency changes in a step of 500 Hz. Under each frequency, all locations (D_1, D_2, D_3) that satisfy equation (6) are obtained and constitute the feasible region in the form of a power isosurface, as shown in Step 1 of Fig. 8.

Step 2 and Step 3 in Fig. 8 show the solving process of the efficiency optimization problem by four algorithms: ACO [8], PSO [11], Cuckoo search (CS) [19], and Grey Wolf Optimization (GWO) [20]. First, under each frequency, with the search ranges of D_1 and D_2 obtained from Step 1, the algorithms generate J (population quantity) groups of (D_1, D_2). Then, for each group of (D_1, D_2), a solution set $(D_{1j}, D_{2j}, \forall D_3)$ distributed on the power isosurface $P_n = P_g$ can be located. From the solution set, the scheme (D_{1j}, D_{2j}, D_{3j}) with the lowest overall loss is recorded as a locally optimal solution and utilized to update the algorithms (e.g., update the lowest objective function value and the global optimum, etc.). Steps 2 through 3 are then iterated until the algorithm converges. In the final, we get four curves of the lowest overall loss with the frequency, where the globally optimal solution of each algorithm can be found. For example, at the operating point $(M = 1, P_S = 700$ W$)$ with $V_1 = 400$ V, Fig. 9 shows the variations of the minimum values of the overall loss obtained by different methods with the frequency.

In Step 4 of Fig. 8, we compare the algorithms' results with the traversal results under 4000 operating conditions to compare the
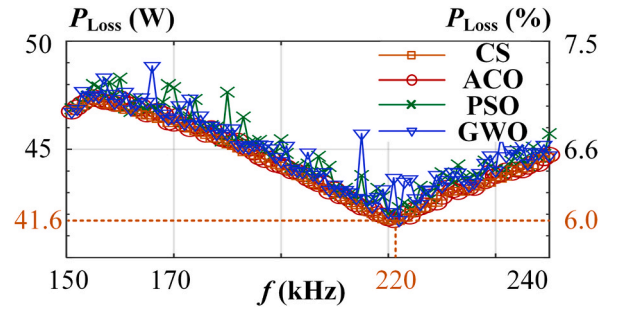
Fig. 9. The variations of the minimum overall loss with the switching frequency at $(M = 1, P_S = 700$ W$)$ with $V_1 = 400$ V.

Table 2
Performance comparison between different optimization methods.

$$MAE = \frac{1}{4000} \sum_{x=1}^{4000} \left| P_{Lossx} - \widehat{P}_{Lossx} \right| \tag{18}$$

$$RMSE = \sqrt{\frac{1}{4000} \sum_{x=1}^{4000} (P_{Lossx} - \widehat{P}_{Lossx})^2} \tag{19}$$

Features	CS	ACO	PSO	GWO	TS
MAE	0.273	0.301	0.379	0.373	0
RMSE	0.308	0.342	0.426	0.431	0
Time (s)	31	29	35	39	>1000

Fig. 8. Framework of the comprehensive-loss-minimized efficiency optimization strategy for the DAB converter with 4-DF modulation.

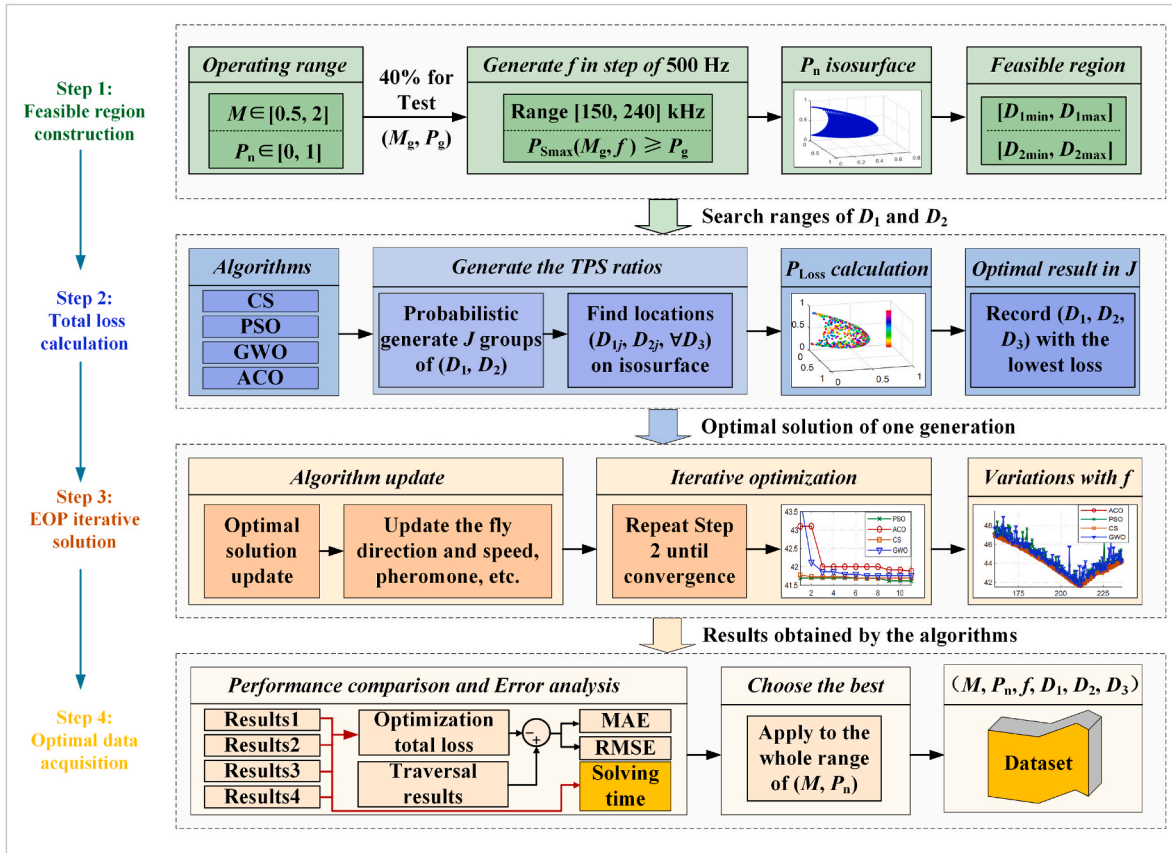optimization performance among different algorithms. Table 2 lists the mean-average error (MAE) and root-mean-square error (RMSE) between the algorithms' results and the traversal results, as well as the average solving time of each algorithm. The MAE and RMSE are given by:where P_{Loss} and $\widehat{P}_{\mathrm{Loss}}$ are the minimum comprehensive loss values obtained by the optimization algorithms and the TS method, respectively. Fig. 9 and Table 2 indicate that the Cuckoo search possesses the best performance due to the lowest overall loss, the stable solving process, and the suitable solving time. Therefore, we choose the Cuckoo search to solve the efficiency optimization problem in the whole operating range, by which 10000 groups of the optimal data $(M_{\mathrm{g}}, P_{\mathrm{g}}, f, D_1, D_2, D_3)$ are obtained. The obtained dataset is used for supervised learning and training of NN.

4.2. 4-DF controller with an NN-aided optimization module

The global efficiency optimization control law for DAB can be expressed as follow:

$$\boldsymbol{Y} = \mathrm{Fun}\,(\boldsymbol{R}) \tag{20}$$

where the optimal modulation vector $\boldsymbol{Y} = (f, D_1, D_2, D_3)$ is a function of the operating condition vector $\boldsymbol{R} = (M, P_{\mathrm{n}})$. Fig. 10 shows the framework of the proposed NN-aided closed-loop controller for DAB, where we use a single hidden-layer NN, which has been proved can approximate any nonlinear functions with any precision [21], to fit the relationship between $\boldsymbol{Y}$ and $\boldsymbol{R}$. The mapping relationship between $\boldsymbol{Y}$ and $\boldsymbol{R}$ determined by NN is expressed as (21):

$$\boldsymbol{Y} = \mathrm{Fun}_2(\mathrm{Fun}_1(\boldsymbol{R} \times \boldsymbol{W}_1 + \boldsymbol{b}_1) \times \boldsymbol{W}_2 + \boldsymbol{b}_2) \tag{21}$$

where $\boldsymbol{W}_x$ and $\boldsymbol{b}_x$ are the connecting weight matrix and the offset matrix, respectively. The hyperbolic tangent sigmoid function Fun_1 and the linear function Fun_2 are the transmission functions of the hidden layer and the output layer of NN, respectively.

The network is trained in MATLAB 2020a software with the Bayesian-Regularization backpropagation algorithm, which can improve the generalization ability of the NN. The main hyperparameter is the cell number of the hidden layer. Aiming to find the appreciative NN scheme, a grid search method is adopted in this paper [22]. Fig. 11 shows the convergence process of the iterative learning of NN with a different number of hidden layer neurons, where the mean-square error (MSE) between the NN output and the dataset is adopted to evaluate the fitting performance. It shows that when the number of the hidden-layer neurons gradually increases to 12, the MSE is much less than the TPS ratios' search accuracy of 0.002 and meets our expectation. The fitting results of NN are shown in Fig. 12, where the optimal data (blue round dots) are generalized into the continuous modulation surfaces of f, D_1, D_2, and D_3, respectively.
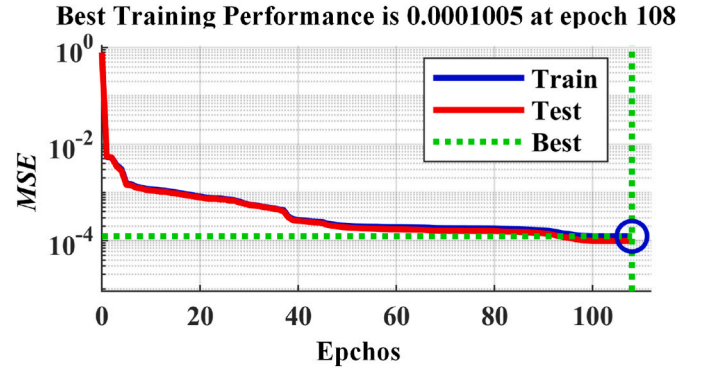

Fig. 11. The convergence processes of the iterative learning of NN with different numbers of hidden layer neurons.
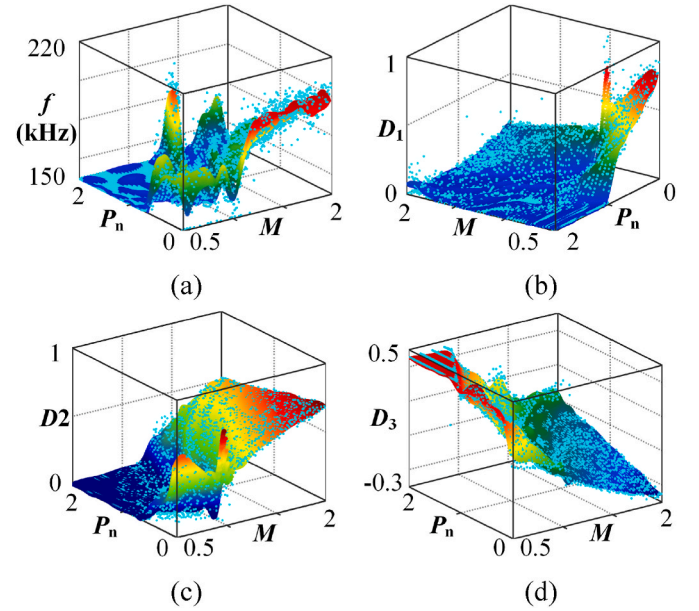
Fig. 12. Fitting results of the NN.

Considering the actual control requirements of DAB, we propose a simple but effective closed-loop controller for DAB. In constant-voltage (CV) control mode, the expected DC voltage gain of DAB (i.e., the first input of NN) is expressed as $M = V_{2\mathrm{ref}}/V_1$, where $V_{2\mathrm{ref}}$ is the voltage command. Meanwhile, the power transmission is determined by the

Fig. 10. Framework of the NN-aided 4-DF closed-loop control strategy for both output voltage/power control and efficiency optimization.

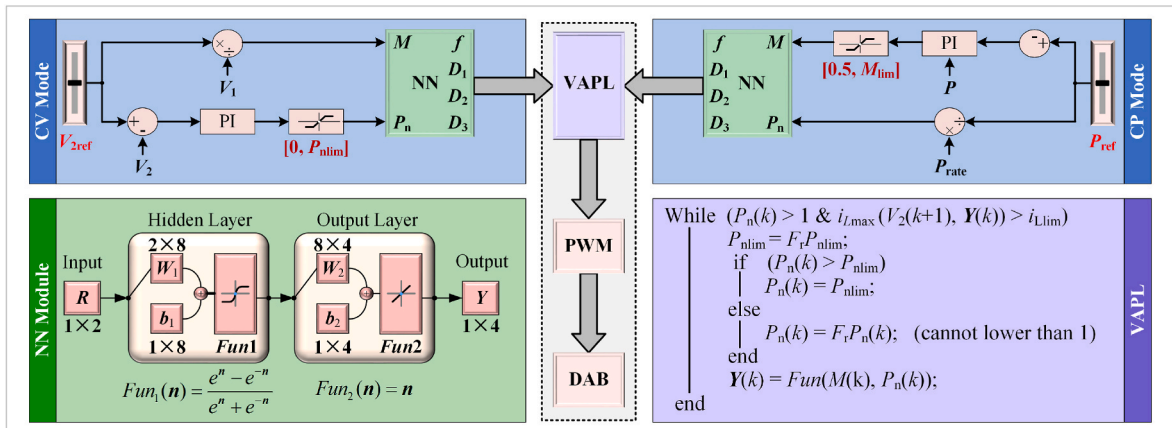load. Therefore, we utilize a PI regulator to produce P_n for NN and regulate the output voltage. When V_2 is lower than $V_{2\text{ref}}$, the PI output P_n will increase, which means that the NN will produce a new modulation scheme to improve the power transmission and the load voltage until $V_2 = V_{2\text{ref}}$. Once the control target is reached, the converter will realize the optimal efficiency operation at the target point. Fig. 10 also illustrates the closed-loop control strategy for DAB in constant-power (CP) mode, where the internal mechanism is similar to the CV mode.

Corresponding to the rated power, the upper limit of P_n is 1. Nevertheless, setting the upper limit to 1 will limit the adjusting speed of the load voltage during dynamic regulation. Therefore, we add a variable-amplitude power limiter (VAPL) into the control loop. The internal mechanism of the VAPL in CV mode is shown in Fig. 10, where k denotes the control cycle number, and $Y(k)$ is the timely modulation scheme produced by NN with the input $P_n(k)$. The current stress of DAB is described by $i_{L\text{max}}$, which can be obtained from formula (1). When $P_n(k) > 1$, the VAPL reduces the limiting amplitude of P_n by predicting whether $i_{L\text{max}}(k+1)$ exceeds the upper limit of i_L. To avoid excessive NN calculation in one control cycle and ensure the real-time performance of the control strategy, the upper limit of P_n is set as 2, and the reduction factor F_r is set as 0.707. When $P_n(k) \leq 1$, $P_{n\text{lim}}$ is reset to 2. By implementing the proposed control strategy, the experimental results are obtained to verify the operating performance of the DAB converter.

5. Experimental results

To verify the feasibility and correctness of the proposed NN-aided 4-DF control strategy, a 1.2 kW experimental prototype is built, of which the photograph and the parameters are given in Fig. 13 and Table 3, respectively. The proposed strategy is implemented by a TMS320F28377D floating-point DSP with a clock frequency of 200 MHz. The control cycle is set as 100µs to meet the bandwidth requirements of DC control.

According to the loss-related functions, three kinds of TPS methods are mainly considered as comparative experiments: The ZVS-oriented strategy in Ref. [6], the $I_{L\text{rms}}$-minimized strategy in Ref. [9], and the reactive-power-minimized strategy in Ref. [11]. Besides, the ZVS-$I_{L\text{rms}}$-oriented strategy considering both ZVS and $I_{L\text{rms}}$ in Ref. [14] is also compared.

The experimental results are organized and introduced as follows: Firstly, subsection 5.1 compares efficiency curves and loss distribution results obtained by different strategies. Then, a detailed comparative analysis among the steady-state waveforms are given in subsection 5.2, followed by a brief disscussion. Finally, subsection 5.3 illustrates the dynamic experimental results of the DAB prototype with the proposed NN-aided controller.
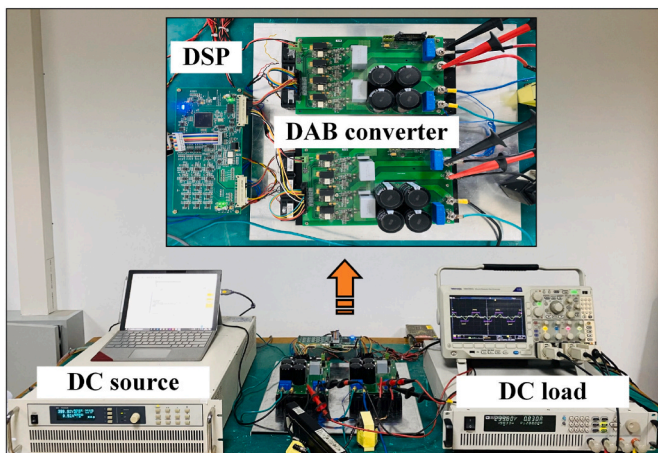

Fig. 13. Photograph of the experimental prototype.

Table 3
Parameters of the DAB experimental prototype.

Main Circuit		HFT	
Variables	Values	Parameters	Values
V_1 (V)	200, 400	K	4.88×10^{-5}
M	[0.5, 1.5]	α	1.38
f_s (kHz)	[150, 240]	β	2.68
L (µH)	41	V_c (cm³)	79
C (µF)	470	ρ_c (kg/cm³)	4.8×10^{-3}
P_{rated} (kW)	1.2	N (turns)	9
N_T	1	l_e (cm)	14.7

5.1. Efficiency comparison

Fig. 14 illustrates the experimental efficiency curves of the ZVS-oriented (ZVS), $I_{L\text{rms}}$-minimized ($I_{L\text{rms}}$), reactive-power-minimized (RP), ZVS-$I_{L\text{rms}}$-oriented (5-DF), and the proposed strategy. With $V_1 = 400$ V, the voltage gains in Fig. 14 (a) and (b) are 0.6 and 1, respectively. It suggests that with the increase of the voltage gain, the overall efficiency of the converter reduces. The converter operates in buck mode in Fig. 14 (a), where the efficiency of the 5-DF strategy is higher than the TPS methods under light and medium power conditions and is the same as the RP TPS strategy in heavy load conditions. With $V_1 = 200$ V, the voltage gains in Fig. 14 (c) and (d) are 1 and 1.5, respectively. When the converter operates in a matched-voltage mode in Fig. 14 (b) and (c), the gap among the efficiency curves of the 5-DF and the TPS strategies becomes small. For the proposed comprehensive-loss-minimized strategy, it achieves the highest efficiency over the entire operating range. Specifically, the maximum efficiency of the proposed strategy is up to 96.4% at $P_S = 1200$ W in Fig. 14 (a) and up to 97.5% at $P_S = 400$ W in Fig. 14 (c), respectively. Furthermore, in the boost mode of Fig. 14. (b), the converter's efficiency is improved more significantly by using the proposed scheme. That is because the excitation voltage of HFT increases in boost mode, and the proportion of core loss more considerable.

Table 4 lists the loss distribution and efficiency obtained by different strategies under seven operating conditions. According to the quantitative loss results, the TPS strategies can improve the efficiency of DAB under some operations but with their limitations. As observed, the efficiency of the ZVS-oriented strategy is the lowest under most conditions. The ZVS-oriented method can ensure the full ZVS among all conditions but cannot minimize the switching loss. That is because, under high input/output voltages and light-load conditions, the full ZVS implementation relies on additional reactive power, leading to higher switching-off and conduction loss. Besides, the $I_{L\text{rms}}$-minimized and reactive-power-minimized strategies cannot achieve full ZVS under light-load conditions.

Furthermore, the loss distribution and the efficiency of the 5-DF strategy are similar to the TPS strategies under most conditions. On the one hand, under medium or high-power operations, the additional two duty cycles will change back to 0.5, and the phase-shift modes provided by the 5-DF modulation are the same as the TPS methods. On the other hand, when the voltages on HFT are matched, all current-stress-based TPS and 5-DF schemes will degenerate to SPS modulation, which is enough to realize the ZVS and minimize the current stress but cannot optimize the loss of HFT. Consequently, under the conditions of heavy-load or matched-voltages, the existing 5-DF strategies cannot improve the converter efficiency to a higher level. In contrast, the proposed comprehensive-loss-based strategy can realize a balance depression among different losses and enhance efficiency over the entire working range. The average efficiency under the proposed modulation strategy in the cases illustrated in Table 4 is 1.09% higher than that of the reactive-power-minimized TPS strategy and 1.05% higher than that of the 5-DF ZVS-$I_{L\text{rms}}$-oriented strategy.
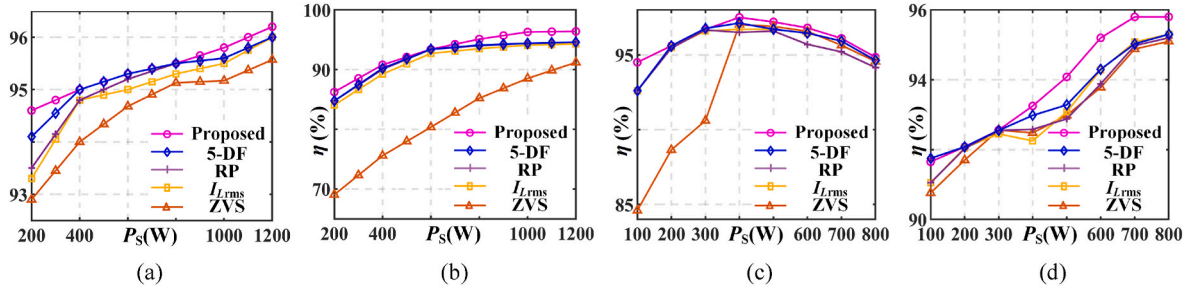
Fig. 14. Experimental efficiency curves of different optimization strategies. (a) Efficiency when $V_1 = 400$ V and $M = 0.6$. (b) Efficiency when $V_1 = 400$ V and $M = 1$. (c) Efficiency when $V_1 = 200$ V and $M = 1$. (d) Efficiency when $V_1 = 200$ V and $M = 1.5$.

Table 4
Quantitative comparison among different efficiency optimization methods.

Number	Conditions	Details	TPS ZVS-Oriented			TPS I_{Lrms}-minimized			TPS RP-minimized			5-DF ZVS-I_{Lrms}-Oriented			Proposed		
1	400 V/400 V1.0, 200 W	f, z, η	150	8	69.02	150	6	84.10	150	6	84.75	150	6	84.75	150	6	86.25
		Losses	9.0	4.8	17.2	10.6	5.1	0.2	9.6	5.3	0.4	9.6	5.3	0.4	8.0	4.8	0.9
2	400 V/400 V1.0, 600 W	f, z, η	150	8	**80.13**	150	6	92.70	150	4	93.40	150	6	93.20	150	4	**93.40**
		Losses	4.2	4.4	11.3	2.1	4.8	0.4	1.9	4.2	0.5	2.0	4.4	0.4	1.9	4.2	0.5
3	400 V/240 V 0.6, 200 W	f, z, η	150	8	92.90	150	6	**93.30**	150	4	93.50	150	8	94.60	150	8	**94.60**
		Losses	3.9	1.6	1.5	4.1	1.5	1.1	3.7	1.6	1.2	3.1	1.2	1.1	3.1	1.2	1.1
4	200 V/200 V 1.0, 100 W	f, z, η	150	8	82.92	150	4	**93.80**	150	4	94.25	150	4	94.10	150	4	**95.31**
		Losses	4.2	3.4	9.5	2.9	3.2	0.1	2.6	3.0	0.1	2.8	3.0	0.1	2.3	2.3	0.1
5	200 V/300 V 1.5, 600 W	f, z, η	150	8	94.20	150	6	93.20	150	8	**94.11**	150	8	94.20	190	8	**95.10**
		Losses	1.8	2.4	1.6	2.7	2.4	1.7	2.1	2.1	1.7	1.8	2.4	1.6	2.2	1.2	1.7
6	400 V/400 V 1.0, 1000 W	f, z, η	150	8	88.52	150	8	94.10	150	6	**94.40**	150	8	94.10	**180**	8	**96.30**
		Losses	2.0	3.9	5.6	1.4	3.9	0.6	1.8	3.0	0.8	1.4	3.9	0.6	1.9	1.6	0.8
7	400 V/300 V 0.75, 400 W	f, z, η	150	8	82.20	150	6	92.14	150	6	92.28	150	7	**92.92**	**180**	6	**94.24**
		Losses	5.0	3.3	9.5	4.14	3.1	0.62	3.8	3.1	0.82	3.38	3.0	0.7	3.5	1.6	0.66

Conditions: V_1/V_2, M, P_S. Losses (%): P_{LossA}, P_{LossB}, P_{LossC}. f, z, η: frequency (kHz), number of ZVS switches, efficiency (%).

5.2. Steady-state characteristics

Corresponding to the working conditions and the colored parts in Table 4, Figs. 15–18 illustrate the measured waveforms of V_H, V_P, and i_L obtained by different phase-shift methods and the proposed strategy. Blue circles and blue dotted circles indicate the switching performance of the leading leg (S_1 and S_2) and the lagging leg (S_3 and S_4) on the primary side, respectively. Red circles and red dotted circles indicate the switching performance of the leading leg (S_5 and S_6) and the lagging leg (S_7 and S_8) on the secondary side, respectively.

5.2.1. Comparison with ZVS-oriented TPS method

Under working condition 1 in Table 4, Fig. 15 (a) and (b) show the results obtained by the ZVS-oriented method and the proposed strategy, respectively. Fig. 15 (a) suggests that all power switches can realize ZVS. However, due to high input/output voltages and light load, the full ZVS implementation depends heavily on reactive power. The high reactive current will cause additional conduction loss and reduce efficiency. In contrast, Fig. 15 (b) shows that quasi zero-current-switching (QZCS)

replaces the ZVS of S_4, but the peak inductor current is reduced from 8 A to 2.4 A. Similarly, Fig. 15 (c) and (d) show the results under condition 2. Compared with Fig. 15 (c), Fig. 15 (d) suggests ZCS replace the ZVS of S_4 and S_5, but the peak inductor current is reduced from 12 A to 2 A. Hence, although the switching loss in Fig. 15 (b) and (d) is slightly higher, the conduction loss is significantly reduced. As listed in Table 4, compared with Fig. 15 (a), the switching and conduction loss in Fig. 15 (b) reduced from 9% to 8% and 17.2%–0.9%, respectively. As a result, the efficiency in Fig. 15 (b) and (d) is higher than in Fig. 15 (a) and (c).

5.2.2. Comparison with I_{Lrms}-minimized TPS method

Fig. 16 (a) and (b) show the measured waveforms of the I_{Lrms}-minimized strategy and the proposed strategy under condition 3, respectively. Fig. 16 (a) indicates that the current stress is well limited at this time, but the soft-switching performance is just like Fig. 15 (b), where full ZVS is unachieved. Compared with Fig. 15 (b), the output voltage is lower, hence the energy required by the secondary switches to realize ZVS decreases. Therefore, under condition 3, full ZVS implementation no longer depends on the reactive current. Fig. 16 (b) shows that the
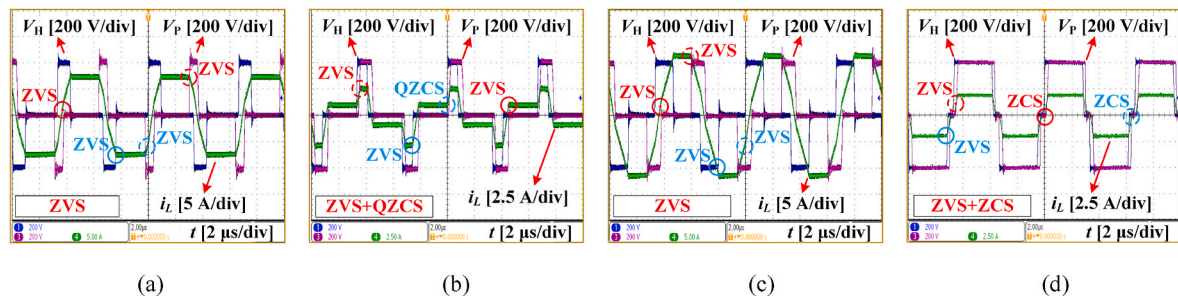

Fig. 15. Experimental waveforms of the ZVS-oriented method and the proposed 4-DF strategy with $V_1 = V_2 = 400$ V. In (a) ZVS-oriented and (b) 4-DF, $P_S = 200$ W. In (c) ZVS-oriented and (d) 4-DF, $P_S = 600$ W.
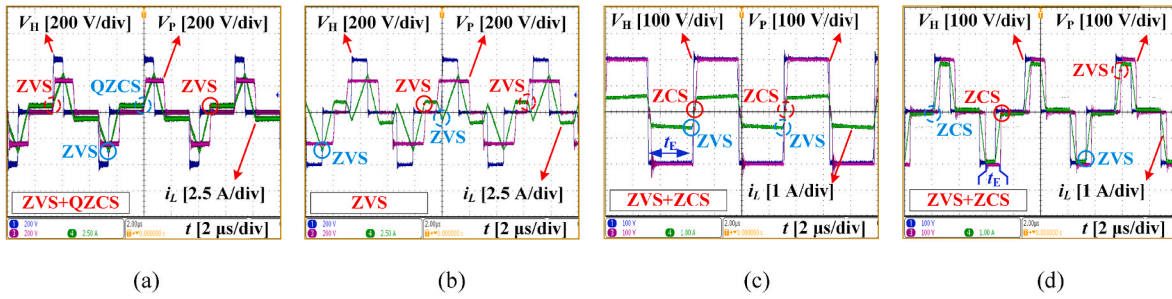
Fig. 16. Experimental waveforms of the I_{Lrms}-minimized method and the proposed 4-DF strategy. In (a) I_{Lrms}-minimized and (b) 4-DF, $V_1 = 400$ V, $V_2 = 240$ V, $P_S = 200$ W. In (c) I_{Lrms}-minimized and (d) 4-DF, $V_1 = V_2 = 200$ V, $P_S = 100$ W.
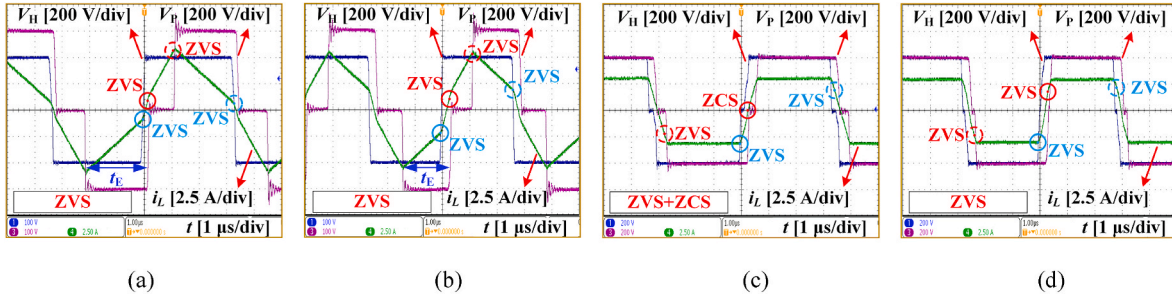

Fig. 17. Experimental waveforms of the reactive-power-minimized method and the proposed 4-DF strategy. In (a) reactive-power-minimized and (b) 4-DF, $V_1 = 200$ V, $V_2 = 300$ V, $P_S = 600$ W. In (c) reactive-power-minimized and (d) 4-DF, $V_1 = V_2 = 400$ V, $P_S = 1000$ W.
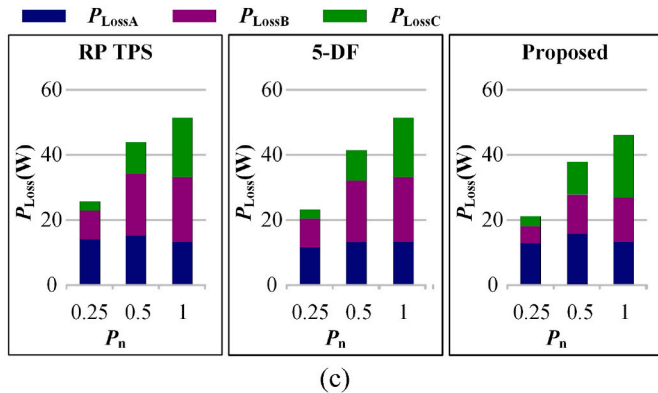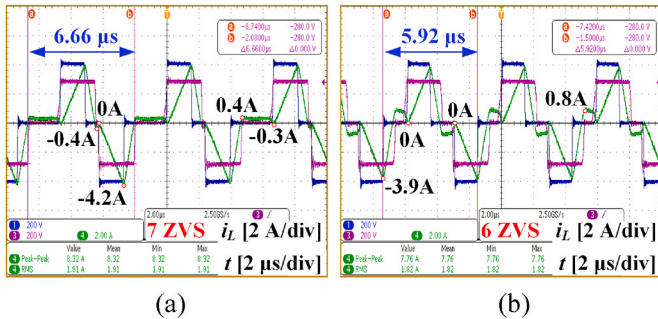

Fig. 18. Comparisons of experimental waveforms and loss breakdown between the ZVS-I_{Lrms}-oriented method and the proposed strategy when $V_1 = 400$ V and $V_2 = 300$ V. Voltage scale: 200 V/div. (a) ZVS-I_{Lrms}-oriented. (b) 4-DF. (c) Loss breakdown.

proposed strategy can realize full ZVS with limited current stress and reactive power, leading to improved efficiency than Fig. 16 (a). Fig. 16 (c) and (d) show the measured waveforms under condition 4. In Fig. 16 (c), the current stress is minimized, and soft-switching is achieved.

However, due to the light-load condition, the proportion of the conduction loss is low, which means minimizing the current stress to improve efficiency has a limited effect. In contrast, with the proposed scheme, a significant reduction in the excitation time t_E of the HFT can be observed in Fig. 16 (d), leading to less core loss according to formula (14). Compared with Fig. 16 (c), the switching and core loss in Fig. 16 (d) reduced from 2.9% to 2.3% and 3.2%–2.3%, respectively, and the efficiency of DAB improved from 93.8% to 95.2%.

5.2.3. Comparison with reactive-power-minimized TPS method

Fig. 17 (a) and (b) are the waveforms of the reactive-power-minimized strategy and the proposed modulation strategy under condition 5, respectively. With a frequency of 150 kHz, the reactive power in Fig. 17 (a) has been minimized, corresponding to a relatively high efficiency of 94.2%. In contrast, the switching frequency in Fig. 17 (b) is optimized to 190 kHz, which reduces the core loss of HFT. Specifically, compared with Fig. 17 (a), the core loss in Fig. 16 (b) reduced from 2.1% to 1.2%, and the efficiency of DAB improved to 95.2%. Similarly, compared with Fig. 17 (c), the frequency in Fig. 17 (d) is optimized to 180 kHz. It suggests that S_5 changes to ZVS from ZCS and the core loss dropped to 1.6% from 3.0%. Therefore, the converter's efficiency improved to 96.3% from 94.4%.

5.2.4. Comparison with ZVS-I_{Lrms}-oriented method

Fig. 18 (a) and (b) are the experimental results obtained by the ZVS-I_{Lrms}-oriented method and the proposed strategy under condition 7, respectively. Fig. 18 (a) suggests that the ZVS-I_{Lrms}-oriented strategy provides an asymmetric current waveform to realize the near-all ZVS. In contrast, although there are only 6 ZVS switches in Fig. 18 (b), the RMS inductor current decreased from 1.91 A to 1.82 A. Moreover, by increasing the switching frequency, the core loss is reduced to 1.6% from 3.0%. As a result, the converter's efficiency is improved from 92.13% to 93.51%.

Fig. 18 (c) shows the loss breakdown of the reactive-power-minimized, the ZVS-I_{Lrms}-oriented, and the proposed strategy at different unified power transmissions when $M = 0.7$. As observed, the

switching loss accounts for a large proportion at light load, and the ZVS-I_{Lrms}-oriented strategy improves the system efficiency by reducing the switching loss. As the power increases, the proportion of core loss gradually increases. The proposed comprehensive-loss-minimized strategy can significantly reduce the core loss with the switching and conduction loss being almost unchanged, so it has the highest global efficiency.

5.3. Dynamic characteristics

Fig. 19 shows the start-up waveforms of the DAB prototype under CV control, where Fig. 19 (a) and (b) correspond to the dynamic processes with and without the proposed VAPL, respectively. It suggests that the DAB converter can operate regularly in the CV mode and has high-efficiency characteristics at the steady-state point. Besides, Fig. 19 (a) suggests a better dynamic performance than Fig. 19 (b) with limited current stress.

Fig. 20 illustrates the dynamic performance for the power transition and voltage command variation under CV control. Fig. 20 (a) shows that the output voltage V_2 and the current i_L can quickly return to the steady-state after P_S is changed from 100 W to 1200 W. Fig. 20 (b) shows desirable dynamic responses of V_2 and i_L when the voltage command step changes from 240 V to 400 V. The steady-state waveforms suggest that the converter can maintain efficient operations like Figs. 15 and 16 before and after the power transition.

Fig. 21 illustrates the dynamic waveforms for the load mutation and power reversal variation under CP control mode. Fig. 21 (a) shows the waveforms when the load is mutated from 48 Ω to 190 Ω with $V_1 = 400$ V and $P_{ref} = 1200$ W. Fig. 21 (b) shows the experimental results when the power command suddenly changes from 400 W to −400 W with $V_1 = V_2 = 200$ V, where the DC output current i_2 is displayed. It can be seen from Fig. 21 (b) that after the power command switching, the inductor current and the voltage change from in-phase to out-of-phase, and V_P changes from lag V_H to lead. The output current i_2 changes from 2 A to −2 A with a short regulation process. The results show that the DAB converter can operate regularly in CP mode. More importantly, the steady-state waveforms appear to have full ZVS performance without reactive power.

6. Brief discussion

Table 5 comprehensively compares the TPS, the 5-DF strategies, and the proposed 4-DF strategy. Under 5-DF modulation, the discrete working modes of the DAB converter are up to 44, which is almost twice that of TPS modulation. In contrast, since the frequency modulation introduced in this paper does not change the operating modes of DAB under the TPS modulation, it maintains the same working complexity as TPS. Furthermore, the proposed algorithm-NN-combined framework provides a convenient direct efficiency optimization method for the DAB converter and is easy to expand and integrate other modulation
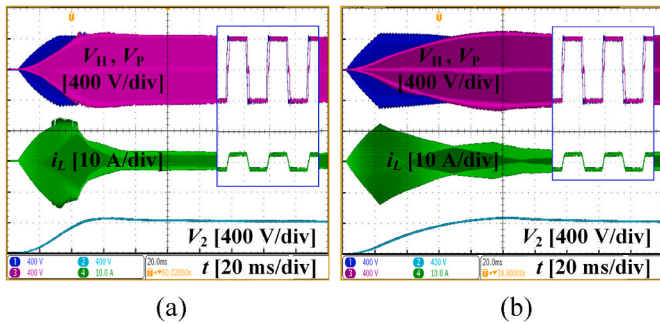

Fig. 19. Start-up waveforms when $V_1 = V_{2ref} = 400$ V and $P_S = 800$ W. (a) With the VAPL. (b) Without the VAPL.
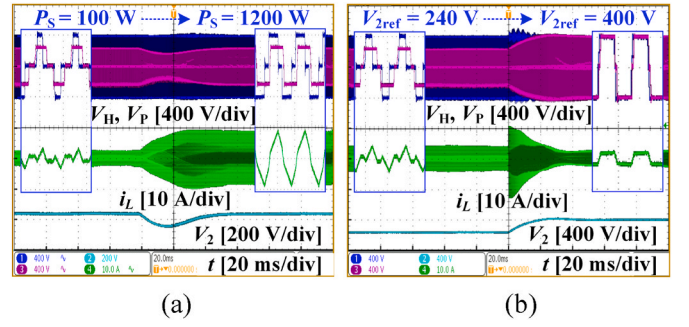

Fig. 20. Dynamic performance for the power transition and voltage command variation under CV control with $V_1 = 400$ V. (a) Power transition from 100 W to 1200 W with $V_{2ref} = 240$ V. (b) Voltage command step from 240 V to 400 V with $R = 288$ Ω.
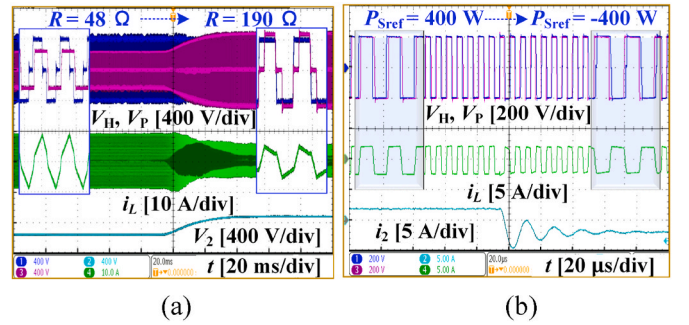

Fig. 21. Dynamic performance for the load mutation and power command step under CP control with $V_1 = 400$ V. (a) Load mutation from 48 Ω to 190 Ω with $P_{ref} = 1200$ W. (b) Power command step from 400 W to −400 W with $V_1 = V_2 = 200$ V.

variables, such as the dead-zone time and the duty cycles in future studies. The 5-DF strategy in Ref. [14] also processes excellent extensibility due to only the objective function needing modification and the frequency modulation requiring consideration. In contrast, once the objective functions in the analytical-based strategies are changed, all analytical formulations need to be constructed and derived again. Therefore, the analytical methods have the lowest extensibilities.

In short, through quantitative analysis and comprehensive comparison with the existing efficiency optimization methods, the proposed comprehensive-loss-minimized 4-DF strategy has more advantages in improving the global efficiency of DAB.

7. Conclusion

In this paper, an NN-aided 4-DF control strategy is proposed to enhance the global efficiency of the DAB converter. A comprehensive loss model considering the nonlinear characteristics of the switching devices and the loss of HFT is established using accurate time-domain analysis. An optimization algorithm-based framework is then proposed to investigate the optimal operating points with the minimum comprehensive loss. On this basis, an NN-aided closed-loop controller is proposed to perform output target control and efficiency improvement for the DAB converter. Finally, a 1.2 kW DAB prototype is built, and the results show that the proposed NN-aided 4-DF control strategy is feasible and superior to the existing methods in efficiency. The conducted studies are summarized as follows.

1) Compared with most existing indirect loss-related cost functions, the established comprehensive loss model reflects the overall loss of the DAB converter more directly and accurately, so it should be used to obtain the optimal global efficiency of the DAB converter. Besides,

Table 5

Comprehensive comparison between the proposed scheme and some typical stratgies

Modulation method	Objective function	EO scheme	Implementation	Extensibility	Optimize core loss	Efficiency Improvement	Discrete Modes	Overall Efficiency
TPS	i_{LRMS} [9]	Analytical	Tabular formulas	Normal	No	Indirect	12	High
	ZVS + i_{LRMS} [10]	Analytical	Tabular formulas	Normal				
	RP [11]	PSO	Tabular dataset	Good				
	RP [12]	Learning	NN	Good				
5-DF	ZVS + i_{Lmax} [13]	Analytical	Tabular formulas	Normal	No	Indirect	22	Higher
	ZVS + i_{LRMS} [14]	PSO	Tabular dataset	Excellent				
This work	Overall loss	CS	NN	Excellent	Yes	Direct	12	Highest

the switching frequency is a necessary and effective modulation DF for optimizing the core loss of the HFT.

2) As a hybrid modulation technique of frequency adjustment and TPS, the proposed comprehensive-loss-minimized efficiency optimization strategy can improve the DAB converter's efficiency over the entire operating range. The loss breakdown results suggest that the existing strategies cannot optimize the loss of HFT, but the proposed strategy can attain the global optimal efficiency by realizing a comprehensive depression among different losses. Compared with the maximum efficiency among the four existing strategies in the illustrated cases, the average overall efficiency of DAB with the proposed strategy has increased by 0.95%.

3) The proposed NN-aided closed-loop controller for the 4-DF DAB converter can synchronously realize both the efficiency improvement and output target control with desirable dynamic characteristics.

Since the inductance may change in practical applications, in the future, the parameter identification method can be studied to obtain the actual inductance value and modify the NN output to further improve the NN-aided controller's applicability.

Author contributions

Hao Zhang: Methodology, Software, Validation, Investigation, Writing – original draft. **Xiangqian Tong**: Resources, Writing – review & editing, Project administration. **Jun Yin**: Software, Validation, Data curation. **Frede Blaabjerg**: Funding acquisition, Writing – review & editing.

Declaration of competing interest

The authors declare that they have no known competing financial interests or personal relationships that could have appeared to influence the work reported in this paper.

Data availability

No data was used for the research described in the article.

References

[1] Lin CC, Wu YF, Liu WY. Optimal sharing energy of a complex of houses through energy trading in the Internet of energy. Energy 2021;220:119613.
[2] Yilmaz Unal, Omer Turksoy, Ahmet Teke. Intelligent control of high energy efficient two-stage battery charger topology for electric vehicles. Energy 2019;186:115825.
[3] McIlwaine Neil, Foley Aoife M, John Morrow D, Al Kez Dlzar, Zhang Chongyu, Lu Xi, Best Robert J. A state-of-the-art techno-economic review of distributed and embedded energy storage for energy systems. Energy 2021;229:120461.
[4] Shao S, Chen L, Shan Z, Gao F, Chen H, Sha D. Modeling and advanced control of dual-active-bridge DC–DC converters: a review. IEEE Trans Power Electron 2022;37(2):1524–47.
[5] Zhao B, Song Q, Liu W, Sun Y. Overview of dual-active-bridge isolated bidirectional DC–DC converter for high-frequency-link power-conversion system. IEEE Trans Power Electron 2014;29:4091–106.
[6] Everts J. Closed-form solution for efficient ZVS modulation of DAB converters. IEEE Trans Power Electron 2017;32(10):7561–76.
[7] Karthikeyan V, Rajesh G. Light-load efficiency improvement by extending ZVS range in DAB-bidirectional DC-DC converter for energy storage applications. Energy 2017;130:15–21.
[8] Zhang H, Tong X, Yin J. Optimal triple-phase-shift controller design of isolated bidirectional DC-DC converter based on ant colony algorithm and BP neural network. In: 43rd annual conference of the IEEE industrial electronics society; 2017. p. 8802–7. Beijing, China.
[9] Tong A, Hang L, Li G, Jiang X, Gao S. Modeling and analysis of a dual-active-bridge-isolated bidirectional DC/DC Converter to minimize RMS current with whole operating range. IEEE Trans Power Electron 2018;33(6):5302–16.
[10] Tang Y, Hu W, Xiao J, Lu Z, Liu Z, Chen Z, Blaabjerg F. A deep Q-Network based optimized modulation scheme for dual-active-bridge converter to reduce the RMS current. Energy Rep 2020;6(9):1192–8.
[11] Shi H, Wen H, Hu Y, Jiang L. Reactive power minimization in bidirectional DC–DC converters using a unified-phasor-based particle swarm optimization. IEEE Trans Power Electron 2018;33(12):10990–6.
[12] Tang Y, Hu W, Cao D, Nie H, Li Y, Chen Z, Blaabjerg F. Artificial intelligence-aided minimum reactive power control for the DAB converter based on harmonic analysis method. IEEE Trans Power Electron 2021;36(9):9704–10.
[13] Mou D, Luo Q, Li J, Wei Y, Sun P. Five-degree-of-freedom modulation scheme for dual active bridge DC–DC Converter. IEEE Trans Power Electron 2021;36(9):10584–601.
[14] Li J, Luo Q, Mou D, Wei Y, Sun P, Du X. A hybrid five-variable modulation scheme for dual-active-bridge converter with minimal RMS current. IEEE Trans Ind Electron 2022;69(1):336–46.
[15] Oggier GG, Ordonez M. High-efficiency DAB converter using switching sequences and burst mode. IEEE Trans Power Electron 2016;31(3):2069–82.
[16] Çelik Doğan, Emin Meral Mehmet. Multi-objective control scheme for operation of parallel inverter-based microgrids during asymmetrical grid faults. IET Renew Power Gener 2020;14(13):2487–98.
[17] Kadri Ameni, Marzougui Hajer, Aouiti Abdelkrim, Bacha Faouzi. Energy management and control strategy for a DFIG wind turbine/fuel cell hybrid system with super capacitor storage system. Energy 2020;192:116518.
[18] Chen B, Lin L, Zhao Z. Calculation of high-power high-frequency transformer's copper loss and magnetic core loss in dual-active-bridge DC-DC converter. Trans China Electrotech Soc 2017;32(22):123–33.
[19] Yuan Z, Wang WQ, Wang HY, Mizzi S. Combination of cuckoo search and wavelet neural network for midterm building energy forecast. Energy 2020;202:117728.
[20] Alirahmi SM, Mousavi SF, Ahmadi P, Arabkoohsar A. Soft computing analysis of a compressed air energy storage and SOFC system via different artificial neural network architecture and tri-objective grey wolf optimization. Energy 2021;236:121412.
[21] Zhang BW, Guo SM, Jin H. Production forecast analysis of BP neural network based on Yimin lignite supercritical water gasification experiment results. Energy 2022;246:123306.
[22] Tang Y, Hu WH, Xiao J, Chen ZY, Huang Q, Chen Z, Blaabjerg F. Reinforcement learning based efficiency optimization scheme for the DAB DC–DC converter with triple-phase-shift modulation. IEEE Trans Ind Electron 2021;68:7350–61.